RESEARCH ARTICLE

Editor's Choice

ADVANCED
ENGINEERING
MATERIALS

www.aem-journal.com

Rapid, Direct Fabrication of Thermochromic Ceramic Composite Sensors via Flash Lamp Annealing

Eren Özmen,* Nicolas Somers, and Mark D. Losego

An inorganic, high-temperature ($\approx$600 °C) thermochromic sensor is synthesized from a chemically bonded ceramic composite. The ceramic composite is composed of thermochromic 10 wt% chromium-doped alumina ($Cr:Al_2O_3$) powder blended with a low-reacting temperature (around 250 °C) phosphate binder, $Al(H_2PO_4)_3$, (aluminum dihydrogen phosphate [ADP]). Cr-doped alumina exhibits thermochromism at high temperatures, typically around 500–600 °C. Previously, infrared (IR) irradiation has been used to successfully convert ADP to an aluminum phosphate ($AlPO_4$) ceramic phase that can bind ceramic components together. Here, an ultrahigh-power (tens of kilowatts per square centimeter) flash lamp annealing (FLA) system is evaluated as an alternative photonic heating process to rapidly transform ADP to this ceramic. While IR lamps require 30 min to fully transform the ADP binder, FLA processes require less than 1 min and provide more dense microstructures, opening opportunities to additively manufacture ceramic components without the need for a post-processing heating step. Final ceramics exhibit reversible thermochromic behavior, transitioning from pink to dark gray as the temperature increases from 25 to 600 °C. Here, the ability to use this technology to fabricate a temperature warning system for heated objects that are not yet emitting significant visible black-body radiation is demonstrated.

1. Introduction

Sintered ceramics and hydraulic cements are two common classes of engineered ceramics.[1,2] Sintered ceramics are synthesized by fusion of compacted powders, which generally requires high-energy manufacturing processes including high temperatures (1500–3000 °C) and/or pressures.[3] Upon sintering, these ceramics fuse particles together by forming primary chemical bonds (covalent/ionic), giving them desired properties such as high wear resistance, high chemical stability, corrosion

resistance, and high hardness. In contrast, hydraulic cements can be formed using low-energy processes in which the inorganic precursors react with water under ambient conditions to form hydrogen bonded inorganic compounds. While hydraulic cements exhibit good mechanical properties and chemical inertness, their engineering performance usually underperforms sintered ceramics because they maintain much of their cohesion through weaker van der Waals forces. Chemically bonded ceramics (CBCs) are an attractive alternative that exists between sintered ceramics and hydraulic cements. CBCs use inorganic binders that can be thermally transformed into primary-bonded ceramic phases at relatively low temperatures (<500 °C), providing a compromise between the higher performance of sintered ceramics and the lower process temperatures of hydraulic cements.

Chemically bonded phosphate ceramics (CBPCs) are composites that are obtained by dissolving an inorganic phosphate binder along with a dense ceramic powder in a solvent, and subsequently reassembling the dissolved components into a new solid structure.[4,5] This acid–base-type CBPC synthesis reaction usually takes place between an anion donor phosphate binder such as phosphoric acid (H_3PO_4), diammonium hydrogen phosphate ($(NH_4)_2HPO_4$, or aluminum dihydrogen phosphate ($Al(H_2PO_4)_3$, aluminum dihydrogen phosphate [ADP]), and a metal oxide like magnesium oxide (MgO) or alumina (Al_2O_3).[6] These systems undergo condensation polymerization reactions that form ceramic phosphate phases bound together by PO_4 tetrahedral linkages. The formation of CBPCs requires low temperatures (<500 °C). Thus, CBPCs have lower energy requirements than sintered ceramics while retaining high chemical resistance, high compressive strength, high abrasion resistance, biocompatibility, and good dimensional and thermal stability, often above 1000 °C.[7] Additionally, CBPCs' versatile chemistry allows functionality to be added to the final product, including corrosion resistance by doping with molybdate or chromate,[8] self-healing capability by doping with cerium oxide,[9] semi-conductivity by doping with indium and its oxides, and thermochromism by doping with vanadium or chromium oxides.[10]

Among these properties, thermochromism stands out for its significant role in monitoring the temperature of engine components in aviation, aerospace, and automotive applications.[11–13] Additionally, thermochromic sensors can serve as security

E. Özmen, N. Somers, M. D. Losego
School of Materials Science and Engineering
Georgia Institute of Technology
771 Ferst Drive NW, Atlanta, GA 30332, USA
E-mail: eozmen3@gatech.edu

The ORCID identification number(s) for the author(s) of this article can be found under https://doi.org/10.1002/adem.202400323.

**ADVANCED
SCIENCE NEWS**

www.advancedsciencenews.com

**ADVANCED
ENGINEERING
MATERIALS**

www.aem-journal.com

sensors to ensure that components operate within their optimal temperature range.[14] Inorganic oxides, such as VO_2, Cr_2O_3, TiO_2, and ZnO are commonly used as optically active dopants to achieve thermochromism in ceramics.[15–17] For example, VO_2 is used to obtain thermochromic smart windows by the replacement of V^{4+} with a small amount of penta- or hexavalent ions.[18,19] However, the low transition temperature (T_c) of VO_2 ($T_c = 68\,°C$) limits its use for high-temperature (>200 °C) sensing applications such as engines and furnaces. The thermochromic color change in Mg–Ni–H thin films deposited by reactive magnetron sputtering has been studied by Željka Raškovic-Lovre et al. as an alternative to low transition temperature materials.[20] Yellow to red color change of these thin films can be observed up to 200 °C. For higher-temperature applications, chromium doping of oxide ceramics is an attractive candidate. For instance, Cr-doped Al_2O_3 can be obtained by replacing Al^{+3} ions with Cr^{+3} ions using solid-state synthesis (SSS). The thermochromism mechanism in chromium-doped alumina derives from ligand-field theory, crystal lattice dynamics, and electronic transitions.[21,22] Ligand field effects force Cr^{3+} ions into constrained octahedral cages formed by O^{2-} ions at lower temperatures, leading to a specific electronic configuration and the existence of the red color due to d-orbitals splitting. At higher temperatures, the lattice expands and Cr^{3+} ions' environment changes to alter its electronic configuration. The competition between Cr^{3+} and Al^{3+} ions for appropriately sized cages, and the temperature-induced expansion, triggers a shift in color from red to green. Thus, color changes from red to pink to green between 200 and 900 °C are possible and depend upon chromium concentration.

Here, we investigate the ability to make CBPC ceramic composites from thermochromic Cr_2O_3-doped Al_2O_3 (Cr:Al_2O_3) powders using a photonic sintering process in a first attempt to demonstrate how this processing method could be used to additively manufacture functional ceramic components. We have previously demonstrated that infrared (IR) light can be used to synthesize and bind CBPC composites.[23] Here, we introduce an even more rapid photonic processing method, flash lamp annealing (FLA), to activate the chemical reactions in these CBPC composites. FLA utilizes a capacitor bank to drive a broadband xenon flash lamp to emit ultrashort pulses (0.1–10 ms) of radiation to rapidly heat surfaces. This method has mainly been used for annealing thin films, sintering metal lines on temperature-sensitive substrates, reflowing solder, activating dopants, and improving the crystallinity of semiconductors.[24–27] With the development of more powerful FLA tools, a limited number of oxide ceramic sintering processes have been reported.[28–33] Here, we seek to combine the lower thermal budget requirements of CBPC synthesis with this advanced and rapid heating technique to form new processing pathways for manufacturing functional ceramic components of arbitrary shapes and designs.

2. Results and Discussion

2.1. Optimization of Thermochromic Cr-Doped Al_2O_3 Powders for Spray-Cast Ceramic Composites

To optimize for color and desired thermochromic response, Cr:Al_2O_3 powders were prepared at varying annealing temperatures

(Figure 1a). As-mixed powders were visually green prior to SSS. Upon heating, the ceramics transformed from green to gray-green color (1000 °C), to gray (1200 °C), and finally to pink (1400 °C). The chemical dissolution of Cr_2O_3 into Al_2O_3 was also tracked using X-ray diffraction (XRD) (Figure 1b). Both the Cr_2O_3 and Al_2O_3 phases are clearly present in the as-mixed powders and at 1000 °C; thus, the gray-green color is likely indicative of residual Cr_2O_3, powder mixed with some Cr:Al_2O_3 at this process temperature. Subsequent annealing to 1200 and 1400 °C results in full dissolution of the Cr_2O_3 into the alumina phase. Figure 1a illustrates the thermochromic response of powders SSS at 1000, 1200, and 1400 °C upon heating to 200, 400, and 600 °C. The 1400 °C SSS powders show the most significant color change when heated from room temperature to 600 °C, transforming from pink ($L = 75.73$, $a* = 9.41$, $b* = -3.08$) to dark gray ($L = 63.28$, $a* = -1.45$, $b* = -4.56$). Interestingly, powders prepared at lower temperatures show minimal change from their initial gray appearance; this non-response is also used later as part of our temperature sensitive device design. These results are consistent with prior studies that used similar Cr:Al_2O_3 weight ratios.[34,35]

While SSS at 1400 °C was successful in achieving a high-temperature thermochromic response, it was found that the powders became significantly more hydrophobic than their preheated counterparts. This hydrophobicity leads to rapid sedimentation in aqueous dispersions, preventing uniform
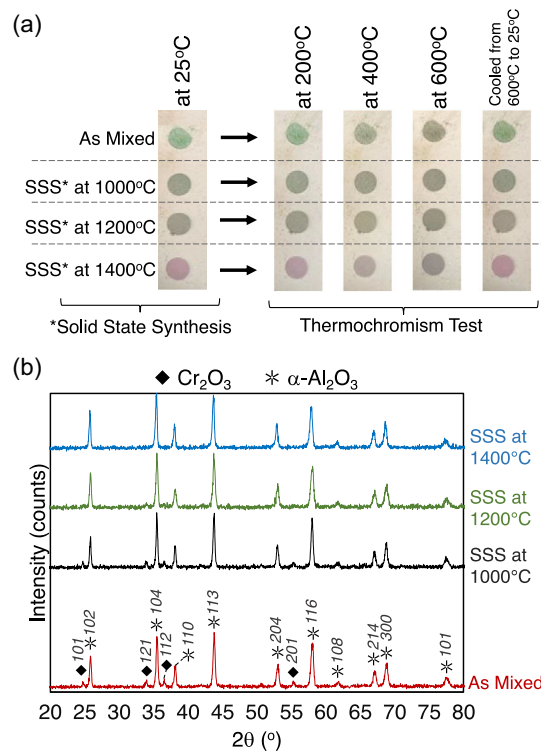
Figure 1. a) Photographic images of 10 wt% Cr-doped Al_2O_3 powders SSS at 1000, 1200, and 1400 °C (left), with corresponding images of these SSS powders subsequently heated to 200, 400, and 600 °C and back to room temperature to demonstrate thermochromic response. b) X-ray diffractograms for 10 wt% Cr-doped Al_2O_3 powder mixtures SSS at 1000, 1200, and 1400 °C, with peaks for α-Al_2O_3 and Cr_2O_3 labeled.

and consistent spray-casting. Several approaches were evaluated to improve dispersion of the powders, and high-energy milling (nano-milling) in an aqueous medium was found to be the simplest and most effective solution. **Figure 2** summarizes this challenge and its solution. Figure 2a demonstrates the sedimentation rates of non-milled and nano-milled SSS 10 wt% Cr:Al$_2$O$_3$–ADP slurries. Sedimentation is observed for the non-milled slurry starting from the first hour. The sedimentation increases over time with 65 vol% liquid phase observed after 24 h. After 72 h, non-milled slurries reach complete sedimentation. In contrast, nano-milled slurries do not exhibit any visual phase separation until 24 h, at which point only 8 vol% liquid phase is visible. Figure 2b plots these sedimentation rates.

Nano-milling of the powders in aqueous medium to reduce the sedimentation rate is found to be essential to allow for delivery approaches (like spraying) that are commensurate with additive manufacturing. Figure 2c provides photographic comparisons of layers sprayed using non-milled and nano-milled powders. Slurries with non-milled powders are nonuniform and show poor wetting on glass substrates. Slurries with nano-milled powders give uniform coverage with layer thicknesses of 100–125 μm.

Nano-milling appears to break apart agglomerates (Figure 2d), reducing their size and their sedimentation rate. When particles interact in concentrated suspensions, their sedimentation rates are determined by hydrodynamic interactions. The friction force (F^{ext}) for a Brownian particle is equal to $6\pi\eta_o\alpha\nu_s$, with η_o the solvent's viscosity, α is the radius of a presumed sphere particle, and ν_s is the sedimentation velocity. This equation can be rewritten as follows

$$\nu_s = \frac{1}{6\pi\eta_o\alpha} F^{ext} \tag{1}$$

During sedimentation test, both samples were kept stable without any external forces such as shaking or centrifugation, thus the only force that applies to particles is the gravity and buoyancy. Thus, the external force F^{ext} can be written as

$$F^{ext} = g\frac{4\pi}{3}\alpha^3\left(\rho_p - \rho_f\right) \tag{2}$$

where ρ_p and ρ_f are the density of particles and the fluid respectively and g is the gravity as of $9.8\,\mathrm{m\,s^{-2}}$. Using this in Equation (1), we can express the sedimentation velocity as

$$\nu_s = g\frac{2\alpha^2}{9\eta_o}\left(\rho_p - \rho_f\right) \tag{3}$$

Here, it is clear that the sedimentation velocity changes with the radius of particles as α^2. Larger particles of identical density, sediment faster than smaller particles. This hypothesis is valid for particles that do not interact with each other nor with the solvent. At early times, this is likely valid. In fact, comparing the initial slopes in Figure 2b (which is the sedimentation velocity), we find a difference of about 270× between the milled (slope = 0.12) to the non-milled (slope = 32.5) powders. This difference is comparable in order of magnitude to the ratio of the squared particle radii imaged in Figure 2d: (65 mm)^2/(5 mm)^2 = 169x, suggesting this initial slope is indicative of gravity-driven particle sedimentation. Interestingly, at longer times, both systems show a change in sedimentation rate that is almost the same. We suspect that this new velocity results from particle–particle interactions or ADP binding in the slurry while the exact mechanism is not clear, this case is also not relevant for this particular use application.

2.2. Comparing IR and FLA Treatments for ADP to AlPO$_4$ Conversion

Successful fabrication of CBPC ceramic composites requires conversion of the ADP precursor to the AlPO$_4$ ceramic phase.
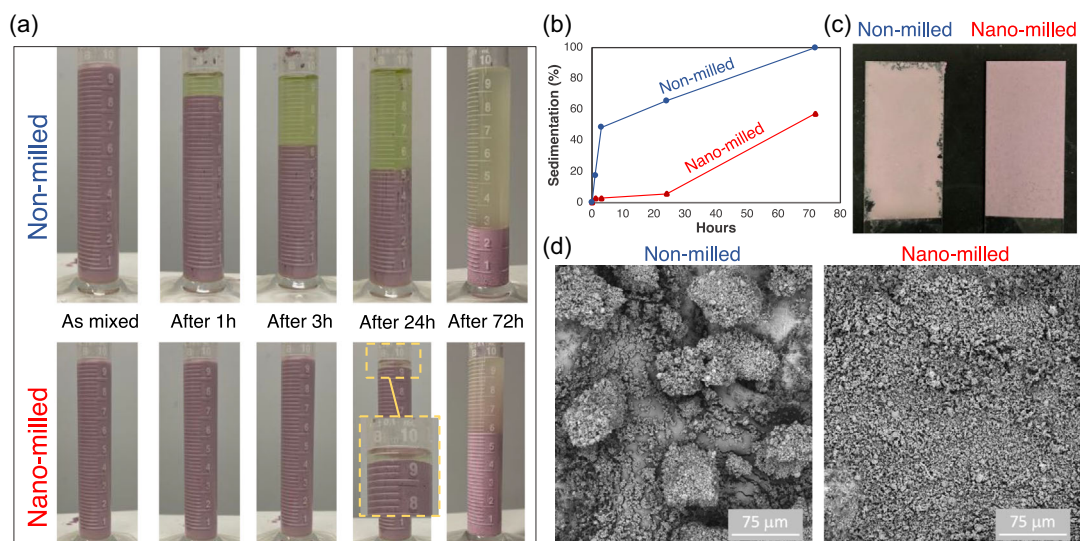
Figure 2. a) Images of non-milled and nano-milled 10 wt% Cr:Al$_2$O$_3$–ADP slurries in graded cylinders, after their preparation, and 1, 3, 24, and 72 h after. b) Comparison of sedimentation rates of nano-milled (▲) and non-milled (•) slurries overtime. c) Photographic images of spray-cast nano-milled and non-milled slurries on glass substrates, d) SEM images of non-milled Cr:Al$_2$O$_3$ powder and nano-milled Cr:Al$_2$O$_3$ dried from slurries on glass slides.

Here, rapid conversion via remote energy delivery is desired to support potential routes to additively manufacture ceramic composite components. Previously, we demonstrated that direct conversion is possible using an IR lamp that can deliver $\approx 0.2\ \mathrm{W\,cm^{-2}}$ of photonic power,[23] but this method can take several to tens of minutes to fully undergo ceramization. Here, we compare IR irradiation to a high-power flash lamp capable of delivering $\mathrm{kW\,cm^{-2}}$ of photonic power. Components processed with both IR irradiation and FLA processing were mechanically robust and had sufficient strength to be handled, moved, and to perform characterization.

Figure 3 presents XRD data for a series of spray-cast Cr:Al_2O_3–ADP layers photonically treated with an IR lamp (Figure 3a) and with the FLA (Figure 3b). These diffractograms confirm that both methods can convert ADP to $AlPO_4$. As-sprayed Cr:Al_2O_3-ADP diffractograms (black patterns in Figure 3a,b) match with the diffraction patterns for $Al(H_2PO_4)_3$ (ADP) and trigonal α-Al_2O_3 (reference pattern ICSD 52 648), as indicated with ✪ and ✳, respectively. The α-Al_2O_3 phase remains consistent throughout all heating processes. The ADP phase, which has its strongest diffraction signal at 24°, converts to the $AlPO_4$ phase labeled with a ♦ as the amount of energy delivered increases.

For IR heating, the diffraction peak for ADP disappears between 304 and 404 $\mathrm{J\,cm^{-2}}$ of energy delivery (or 20–30 min of irradiation). For FLA heating, the ADP diffraction peak disappears between 279 and 327 $\mathrm{J\,cm^{-2}}$ (both only 48 s of process time). Interestingly, in both cases, the $AlPO_4$ diffraction peak emerges above $\approx 300\ \mathrm{J\,cm^{-2}}$ of energy delivered, and the diffraction intensity increases with increasing delivered energy, indicative of increasing crystallinity or amount of the phase. We detect similar structural changes consistent with the conversion of ADP to $AlPO_4$ in IR spectroscopy. We note that FLA heating of this slurry is assisted by the fact that the ceramic powder is thermochromic and absorbs light at optical wavelengths, allowing for heating of the material. For cases where slurry compositions create a white appearance (mostly reflective to optical wavelengths), FLA heating has been observed to be much less efficient.

While diffraction and spectroscopy provide direct evidence of the structural and chemical transformations occurring, we find that operationally it is important to react "sufficiently" to avoid
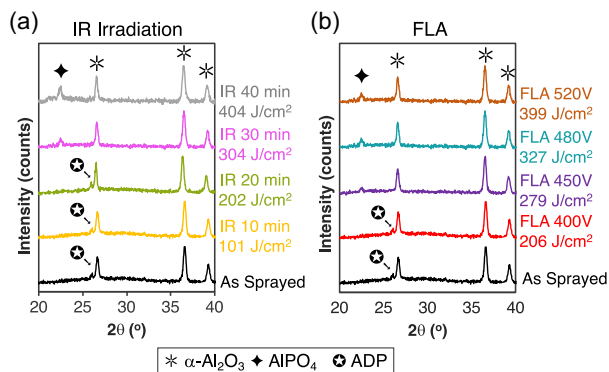
Figure 3. XRD diffractograms for a) IR-irradiated, and b) FLA-processed Cr:Al_2O_3–ADP layers. Miller indices of peaks at $2\theta = 22.6$ (♦), 26.3 (✪), 26.7 (✳), 36.5 (✳), and 39.3 (✳) are 211, 101, 102, 104, and 110, respectively.
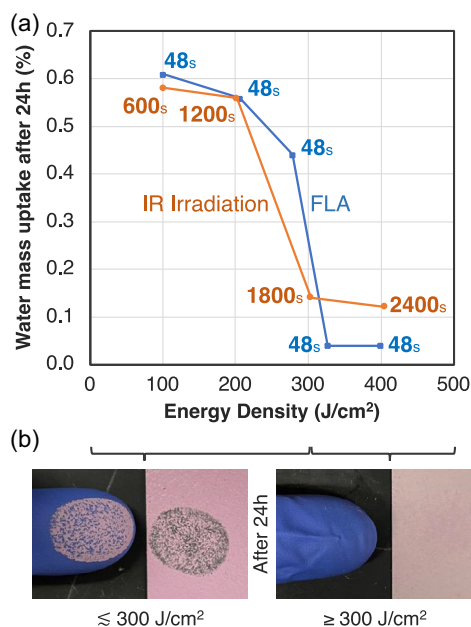

Figure 4. a) Water mass uptake of Cr:Al_2O_3–ADP layers that are processed with FLA at 350, 400, 450, 480, and 520 V of lamp power, and IR processed for 10, 20, 30, and 40 min. b) Photographs of a touch test to show how hydration degrades the material after 24 h of ambient exposure, comparing materials processed at <300 $\mathrm{J\,cm^{-2}}$ (left, degraded) to those process at >300 $\mathrm{J\,cm^{-2}}$ (right, not degraded).

ADP's hygroscopic sorption of humidity from the atmosphere. If not "sufficiently" reacted, then composites will sorb water and lose mechanical integrity. Thus, quantitative measurements of gravimetric water uptake in the final CBPC ceramic composite provide additional characterization of the fractional transformation of ADP to $AlPO_4$ and a practical assessment of when the composite is fully stable. To quantify this behavior, we measure the mass uptake of the composites when left for 24 h in an ambient lab environment of 54% relative humidity. The measured mass uptake is presumably water sorption. Figure 4 plots this water mass uptake for composites prepared at similar IR exposure times and FLA energy densities presented in the XRD data of Figure 4. As expected, with increased energy delivery, composites sorb less water. Interestingly, for both irradiation methods, abrupt drops in water sorption are observed between 200 and 300 $\mathrm{J\,cm^{-2}}$, demonstrating some consistency in the energy necessary for ceramic conversion in this system irrespective of the photonic energy delivery method. Two other key observations are: 1) that at "full conversion" the FLA system reaches an overall lower water mass uptake than the IR heated system; and 2) the time to reach this "full conversion" is almost two orders of magnitude shorter (48 vs ≈ 2000 s). The speed of this FLA process is particularly notable as it suggests a pathway to practical single-step additive manufacturing.

2.3. Effect of IR and FLA Processing on the Microstructure of Cr:Al_2O_3–ADP Layers

Figure 5 shows top surface and cross-sectional optical and SEM micrographs of Cr:Al_2O_3–ADP layers processed with IR
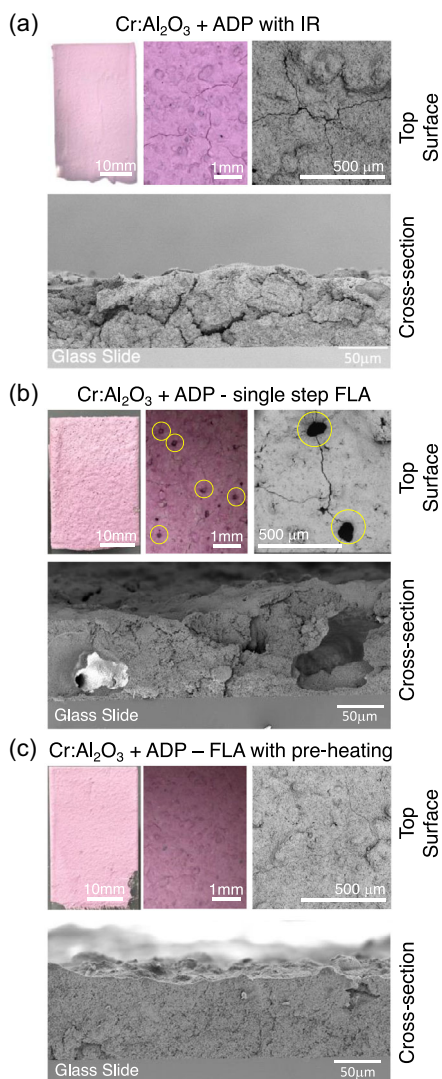
Figure 5. Top surface (photograph, optical image, and SEM) and cross-sectional SEM images of $Cr:Al_2O_3$–ADP layers processed with a) IR irradiation for 20 min, b) FLA using only high energy pulses (30×10.3 J cm^{-2} pulses), c) FLA processed with a preheating step (10×1.1 J cm^{-2} pulses) followed by 30×10 J cm^{-2} pulses.
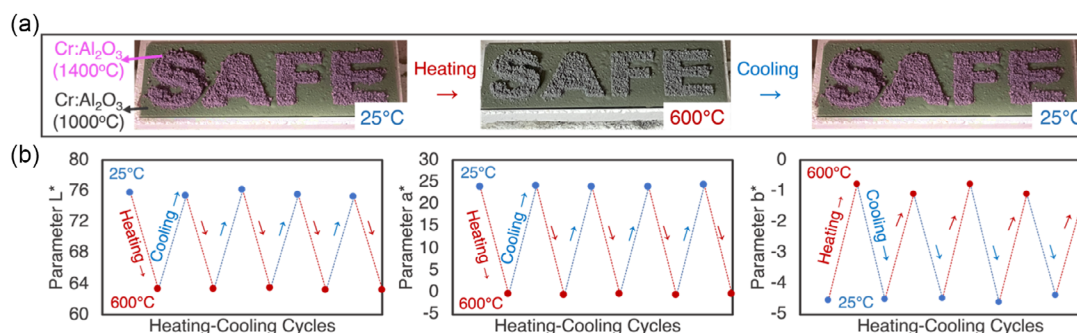
irradiation (Figure 5a) and FLA (Figure 5b,c). The top surface of IR processed layers are reasonably homogenous but consist of cracks as shown in Figure 5a. These cracks most likely occur due to volume shrinkage during dehydration and ceramization. As-sprayed layers are about 100–125 μm thick but consolidate to as thin as 45–55 μm upon irradiation. Cross-sectional images reveal significant cracking and discontinuities in the bulk of the IR-heated layers as well. Figure 5b shows $Cr:Al_2O_3$–ADP layers that are processed with FLA using a sequence of 30 pulses of 10.3 J cm^{-2} for a total delivery of ≈309 J cm^{-2}. This direct energy deposition heats up the sample rapidly and caused holes in the structure (marked with yellow circles in Figure 5b), most likely due to rapid physical water evaporation. These outlet holes are continuous through the entire layer with diameters changing from 20 to 80 μm. Figure 5c shows $Cr:Al_2O_3$–ADP layers that are

processed with a preheating step (10×1.1 J cm^{-2} pulses) to evaporate any physical water trapped in the layers. These layers are then subsequently processed with higher energy FLA pulses (total energy of 300 J cm^{-2}), identical to those used in Figure 5b. Both top and cross-sectional microstructures show good homogeneity and consolidation with no indications of major defects nor cracking. The microstructure of as-sprayed layers is dense without any porosity and consists of two phases (dark part is ADP and bright part is alumina) as shown in Figure S1, Supporting Information. When compared to previously mentioned microstructures obtained using IR and FLA methods, the FLA with preheating has the success of preserving the dense microstructure of as-sprayed layers with its controllable heat transfer and water evaporation. This comparison shows the importance of parameter and strategy optimization during additive manufacturing approaches.

2.4. Demonstration of an Additively Manufactured Thermochromic Sensor

To demonstrate feasibility of this approach for additive manufacturing we have spray-cast a patterned thermochromic CBPC composite layer ($Cr:Al_2O_3$ SSS at 1400 °C) onto a non-thermochromic layer ($Cr:Al_2O_3$ SSS at 1000 °C). Using the color analysis from Figure 1, we have chosen compositions such that the layers will have different colors at room temperature but nearly the same color at elevated temperatures (>600 °C). **Figure 6**a shows the results of this demonstration. Here, we print the word "SAFE" in thermochromic composite to indicate the component is safe to touch. At room temperature, "SAFE" is highlighted in pink letters ($L^* = 76.28$, $a^* = 24.45$, $b^* = -4.56$) on a gray background ($L^* = 63.73$, $a^* = -0.41$, $b^* = -0.73$), which allows for easy visual identification of the message. When heated to 600 °C, the pink letters turn dark gray ($L^* = 75.54$, $a^* = 24.31$, $b^* = -4.38$), making them visually "disappear" into the background. As the color separation is harder to distinguish, the system indicates it is no longer safe to touch due to its high temperature. This embedding method can also be employed to monitor the surface temperature of engineering equipment as a thermal sensor, particularly in cases where maintaining a temperature around 600 °C is crucial for efficient functioning and the temperature may not yet be visible due to black-body emission. Conceivably, other compositions could be synthesized with varying thermochromic temperatures to provide a range of temperature indicators in a single device.

Importantly, this color change is reversible, and when the coatings cool back down to room temperature, the thermochromic layer returns to its pink color (right most image in Figure 6a). To quantify this reversibility, Figure 6b–d plots the L^*, a^*, and b^* color values measured from the "SAFE" letters upon cycling between 600 and 25 °C over five cycles. Parameter L^* changes by 18%, while parameters a^* and b^* changes by 25% and 7% respectively between 25 and 600 °C. Usually, it is expected that pink has CIELAB color properties around $L^* = 60$–80, $a^* = 20$–30, and $b^* = 0$–5, and gray $L^* = 50$, $a^* = 0$, and $b^* = -1$.[34] The most significant change is in the a^* parameter, which indicates the redness, consistent with the color change from pink to gray. Importantly, upon cycling,

**ADVANCED
SCIENCE NEWS**

www.advancedsciencenews.com

**ADVANCED
ENGINEERING
MATERIALS**

www.aem-journal.com

Figure 6. a) Glass slides prepared with letters of 10 wt% Cr:Al$_2$O$_3$–ADP (SSS at 1400 °C) and surrounding media of 10 wt% Cr:Al$_2$O$_3$–ADP (SSS at 1000 °C). Color change of letters at 600 °C makes them disappear within the background, warning users that it is no longer safe to touch. b) L*, a*, and b* color values of letters during five cycles of heating and cooling between 25 and 600 °C.

these color parameters generally return to similar values, indicating good reversibility of this thermochromic device.

3. Conclusion

This study shows the feasibility of processing CBPCs with reversible thermochromic properties using photonic annealing methods in a process flow consistent with additive manufacturing. Phase analysis confirms that the remote photonic energy can transform the ADP binder into an AlPO$_4$ ceramic phase that binds the thermochromic powders together. Interestingly, the quantity of energy needed to achieve "full conversion" of ADP to AlPO$_4$ is approximately the same for both IR irradiation and FLA, about 300 J cm^{-2}. However, FLA can accomplish this energy delivery in nearly two orders of magnitude shorter time, making it even more amenable for rapid prototyping. By understanding the thermochromic color changes of Cr:Al$_2$O$_3$ under varying SSS conditions, we manufactured a simple, patterned thermochromic device to demonstrate the potential for this technology. Future work will need to optimize similar slurries for integration with higher resolution printing methods like inkjet printing and aerosol jet printing. Additionally, stacking of multiple layers and understanding their interaction, both internally and in conjunction with the FLA method, will bring a new approach to rapid additive manufacturing.

4. Experimental Section

Preparation of Cr-Doped Al$_2$O$_3$ Thermochromic Slurries: SSS of Cr$_2$O$_3$–Al$_2$O$_3$ Powders: Equal amounts of two different nanosized α-Al$_2$O$_3$ powders (30 and 100 nm 99.5% purity, sourced from MSE Supplies) were mixed with 10 wt% Cr$_2$O$_3$ powder in an analog tube roller. The SSS of these components was carried out in an electric furnace at 1000, 1200, and 1400 °C to study the influence of temperature on α-Al$_2$O$_3$–Cr$_2$O$_3$ interaction. After the SSS was completed, each powder mixture was uniaxially pressed into pellet form. Pure Cr:Al$_2$O$_3$ pellets were used to optimize the thermochromic response.

Thermochromic Slurry Preparation: Slurries of thermochromic ceramic powder and ADP binder were prepared to make thermochromic composites that could be easily printed. The inorganic phosphate binder Al(H$_2$PO$_4$)$_3$ (ADP) was supplied in powder form (>95.0%, Sigma Aldrich), and a 35 wt% aqueous solution was prepared by dissolving the ADP in deionized water for 12 h with continuous stirring. ADP showed

a significant affinity for humidity in the air, due to the high number of hydroxyl groups in its structure. When the powder of ADP was exposed to the ambient lab environment, the hydroxyl groups reacted with water to soften the ADP into a jelly form. The ADP converted into ceramic AlPO$_4$ was not hygroscopic. Thus, a strong relationship existed between the successful conversion of ADP to AlPO$_4$ and the amount of water mass uptake for this material. We subsequently used this relationship to understand the amount of ADP to AlPO$_4$ conversion.

A thermochromic ceramic slurry was prepared by mixing 60 g of the ADP solution with 15 g of Cr:Al$_2$O$_3$ powder (SSS at 1400 °C). The slurry was then milled in a high energy ball mill (RETSCH E-max) with speeds of 1200 min^{-1} for 2 h using stainless steel grinding jars and balls (with radius changing from 0.1 to 25 mm). The final molar ratio of ADP to Al$_2$O$_3$ was 1.3:1, and volume ratios of ADP and alumina was ≈37 and 7 vol%, respectively. A high-volume low-pressure air-spray gun (Master AirBrush) was then used to spray-cast these slurries onto soda-lime glass slides and stainless-steel substrates. Spray-cast layers were preserved in a drying chamber at 70 °C until further processing either by FLA or IR irradiation.

Thermochromic Sensor Design: To design a thermochromic high-temperature sensor, a mask (76 × 26 × 2 mm) with hollow "S A F E" letters was printed using the fused filament deposition method. First, a bare borosilicate microscope glass slide (76 × 26 × 2) was spray-coated with Cr:Al$_2$O$_3$ (SSS at 1000 °C)—ADP slurry and this layer were photonic cured using FLA. Then, the FDM-printed mask was placed on top of this layer and the hollow "S A F E" letters were filled with spray-casting using the Cr:Al$_2$O$_3$ (SSS at 1400 °C)—ADP slurry. This second layer was then also cured with FLA.

IR and FLA Processing: After preparing slurries and spray-casting on substrates, each deposited layer was initially dried in an oven at 60 °C for 1 h to set the same hydration level and then photonically cured with either an IR lamp (*Solary 1600 W IR lamp*) or an FLA system (PulseForge, Invent).

IR irradiation was performed for 10, 20, 30, or 40 min at a distance of 5 cm to investigate the impact of processing time on the condensation–polymerization of the Al(H$_2$PO$_4$)$_3$ binder. An optical power meter (*Newport 1830-C*) was used to measure the actual power delivered by the IR lamp onto the samples. The energy density transferred to the sample was calculated using the formula

$$\text{Energy} = \frac{\text{Power (Watts)} \times \text{Time (Seconds)}}{3.14} [\text{J cm}^{-2}] \quad (4)$$

where the power is the reading from the optical power meter in Watts for a 5 cm distance, time is the processing time in seconds, and 3.14 cm^2 is the surface area of the probe. The calculated energy densities for processing times of 10, 20, 30, and 40 min were 101, 203, 304, and 405 J cm^{-2}, respectively.

Other Cr:Al$_2$O$_3$-ADP layers were photonically cured with an FLA system. The distance between xenon lamp and sample surface was set to 11 mm.

The photonic pulse sequence was freely adjusted. It was found that an initial sequence of low-energy pulses (10 flashes with 100 V or 1.1 J cm^{-2} of lamp power for a total energy of at 11 J cm^{-2}) was important to first remove physically absorbed water prior to driving ceramization. This "drying step" was followed by higher energy pulses at a range of lamp voltages varying from 400 to 520 V, each with 30 repetitions, providing energy densities of 207, 279, 327, and 399 J cm^{-2} respectively, paralleling those provided by the IR lamp. Since energy delivery was varied by lamp voltage, the duration of each FLA process was able to be kept constant at 48 s.

Chemical and Physical Characterization: Crystallographic properties of powders and cured layers were studied with an ARL Equinox 100 X-ray diffractometer (Cu Kα = 1.5406 Å) with an angle of incidence set to 8°. Water sorption was also used as a measure of the fractional conversion of ADP to AlPO$_4$. For these tests, samples were weighed just after IR or FLA, and 24 h after exposure to room atmosphere with 54% humidity. The difference between two measurements was considered as the capacity of water mass uptake, indicative of the amount of unreacted, hygroscopic ADP remaining in the material.

A digital microscope (Leica DVM6) was used to take images of top surface and cross section of Cr:Al$_2$O$_3$–ADP layers before and after IR and FLA curing. Scanning electron microscopy (SEM) was performed on a benchtop SEM (Phenom ProX G5) using 10 and 15 kV in image mode. Then specimens were affixed to aluminum stubs using conductive carbon tape and subsequently coated with a 1.5–5 nm layer of gold using sputtering method prior to imaging.

An Avantes fiber optic UV/Vis spectrometer (Avaspec-ULS2048CL-EVO) with an integrating sphere attachment for diffuse reflectance analysis was used to measure the color the thermochromic ceramics. Pellets were heated to 200, 400, and 600 °C and their thermochromic color change was tracked visually and with the Avantes CIE $L*a*b$ colorimetry software. The CIELAB color space, as defined by the International Commission on Illumination (CIE), provided a standardized way to numerically quantify the color of an object. $L*$, $a*$, and $b*$ represent the CIE Lab* color parameters.[36] Pellets were then cooled to room temperature to study the reversibility of the color change.

Supporting Information

Supporting Information is available from the Wiley Online Library or from the author.

Conflict of Interest

The authors declare no conflict of interest.

Data Availability Statement

The data that support the findings of this study are available from the corresponding author upon reasonable request.

[1] P. B. Parikh, *Trans. Indian Ceram. Soc.* **1995**, *54*, 179.

[2] D. M. Roy, *Science* **1987**, *235*, 651.

[3] J. E. Marion, C. H. Hsueh, A. G. Evans, *J Am. Ceram. Soc.* **1987**, *70*, 708.

[4] A. S. Wagh, in *Chemically Bonded Phosphate Ceramics*, Elsevier, New York **2016**, pp. 1–16.

[5] A. S. Wagh, *ISRN Ceram.* **2013**, *2013*, 983731.

[6] A. S. Wagh, S. Y. Jeong, *J. Am. Ceram. Soc.* **2003**, *86*, 1838.

[7] A. Zezulova, M. Dzurov, M. T. Palou, *J. Phys.: Conf. Ser.* **2022**, *2341*, 012005.

[8] Y. Liu, D. Bian, Y. Zhao, *J. Sol-Gel Sci. Technol.* **2019**, *89*, 403.

[9] F. Rebillat, in *Advances in Ceramic Matrix Composites*, Elsevier, Amsterdam, The Netherlands **2014**, pp. 475–514.

[10] G. Pérez, A. Guerrero, in *Smart Nanoconcretes and Cement-Based Materials*, Elsevier, Madrid **2020**, pp. 403–418.

[11] M. A. White, M. LeBlanc, *J. Chem. Educ.* **1999**, *76*, 1201.

[12] K. R. Karpagam, K. S. Saranya, J. Gopinathan, A. Bhattacharyya, *J. Text. Inst.* **2016**, *108*, 1122.

[13] S. Wu, H. Sun, M. Duan, H. Mao, Y. Wu, B. Lin, *Cell Rep. Phys. Sci.* **2023**, *4*, 101370.

[14] A. Hakami, S. S. Srinivasan, P. K. Biswas, A. Krishnegowda, S. L. Wallen, E. K. Stefanakos, *J. Coat. Technol. Res.* **2022**, *19*, 377.

[15] B. Zhang, C. Xu, G. Xu, S. Xiang, Y. Zhu, *Opt. Mater.* **2018**, *86*, 464.

[16] H. Liu, L. Yuan, X. Wu, X. Hou, M. Tang, C. Hou, H. Chen, S. Feng, *J. Mater. Chem. C* **2020**, *8*, 9615.

[17] G. Ferro, D. Carole, F. Cauwet, L. Acher, H. Ji, R. Chiriac, F. Toche, A. Brioude, *Opt. Mater.: X* **2022**, *15*, 100167.

[18] A. Huang, Y. Zhou, Y. Li, S. Ji, H. Luo, P. Jin, *J. Mater. Chem. A* **2013**, *1*, 12545.

[19] Y. Gao, C. Cao, L. Dai, H. Luo, M. Kanehira, Y. Ding, Z. L. Wang, *Energy Environ. Sci.* **2012**, *5*, 8708.

[20] Ž. Rašković-Lovre, T. Mongstad, S. Karazhanov, S. Lindberg, C. C. You, S. Deledda, *Mater. Lett.* **2017**, *188*, 403.

[21] D. K. Nguyen, Q.-V. Bach, B. Kim, H. Lee, C. Kang, I.-T. Kim, *Mater. Chem. Phys.* **2019**, *223*, 708.

[22] K. Sone, Y. Fukuda, in *Inorganic Thermochromism*, Inorganic Chemistry Concepts, Vol. 10, Springer, Berlin, Heidelberg **1987**.

[23] N. Somers, A. Montón, E. Özmen, M. D. Losego, *J. Am. Ceram. Soc.* **2024**, *107*, 36.

[24] R. A. McMahon, M. P. Smith, K. A. Seffen, M. Voelskow, W. Anwand, W. Skorupa, *Vacuum* **2007**, *81*, 1301.

[25] S. Prucnal, T. Shumann, W. Skorupa, B. Abendroth, K. Krockert, H. J. Möller, *Acta Phys. Pol., A* **2011**, *120*, 30.

[26] Y. Endo, T. Fujiwara, K. Ohdaira, S. Nishizaki, K. Nishioka, H. Matsumura, *Thin Solid Films* **2010**, *518*, 5003.

[27] K. Mallikarjuna, M. Shinde, A. Kumar, J. Ryu, H. Kim, *ACS Sustainable Chem. Eng.* **2021**, *9*, 14559.

[28] E. Gilshtein, S. Pfeiffer, M. D. Rossell, J. Sastre, L. Gorjan, R. Erni, A. N. Tiwari, T. Graule, Y. E. Romanyuk, *Sci. Rep.* **2021**, *11*, 3536.

[29] É. O'Connor, M. Halter, F. Eltes, M. Sousa, A. Kellock, S. Abel, J. Fompeyrine, *APL Mater.* **2018**, *6*, 121103.

[30] J.-S. Park, D.-J. Kim, W.-H. Chung, Y. Lim, H.-S. Kim, Y.-B. Kim, *Sci. Rep.* **2017**, *7*, 12458.

[31] S. H. Shin, J.-S. Park, H. Lee, S.-W. Kong, J. Park, Y. Won, Y.-B. Kim, *Coatings* **2019**, *10*, 9.

[32] A. G. Attallah, S. Prucnal, M. Buttering, E. Hirschmann, N. Koehler, S. E. Schulz, A. Wagner, M. O. Liedke, *Sci. Rep.* **2023**, *13*, 7765.

[33] H. Elsayed, M. Picicco, A. Dasan, J. Kraxner, D. Galusek, E. Bernardo, *Ceram. Int.* **2020**, *46*, 25299.

[34] P. M. Lewis, K. N, D. Hebbar N, K. S. Choudhari, S. D. Kulkarni, *Curr. Appl. Phys.* **2021**, *32*, 71.

[35] D. Nguyen, H. Lee, I.-T. Kim, *Materials* **2017**, *10*, 476.

[36] B. Hill, T. Roger, F. W. Vorhagen, *ACM Trans. Graph.* **1997**, *16*, 109.